

# Perfect reconstruction of sparse signals with piecewise continuous nonconvex penalties and nonconvexity control

Ayaka Sakata<sup>1,2</sup> and Tomoyuki Obuchi<sup>3</sup>

<sup>1</sup>Department of Statistical Inference & Mathematics, The Institute of Statistical Mathematics, Midori-cho, Tachikawa, Tokyo 190-8562, Japan

<sup>2</sup>Department of Statistical Science, The Graduate University for Advanced Science (SOKENDAI), Hayama-cho, Kanagawa 240-0193, Japan

<sup>3</sup>Department of Mathematical & Computing Science, Tokyo Institute of Technology, Ookayama, Meguro-ku, Tokyo 152-8552, Japan

E-mail: <sup>1,2</sup>ayaka@ism.ac.jp, <sup>3</sup>obuchi@c.titech.ac.jp

**Abstract.** We consider compressed sensing formulated as a minimization problem of nonconvex sparse penalties, Smoothly Clipped Absolute deviation (SCAD) and Minimax Concave Penalty (MCP). The nonconvexity of these penalties is controlled by nonconvexity parameters, and  $\ell_1$  penalty is contained as a limit with respect to these parameters. The analytically derived reconstruction limit overcomes that of  $\ell_1$  and the algorithmic limit in the Bayes-optimal setting, when the nonconvexity parameters have suitable values. For the practical usage, we apply the approximate message passing (AMP) to these nonconvex penalties. We show that the performance of AMP is considerably improved by controlling nonconvexity parameters.

## 1. Introduction

A signal processing scheme for reconstructing signals through linear measurements, when the number of measurements is less than the dimensionality of the signals, is known as compressed sensing (or compressive sensing) [1, 2]. Let  $\mathbf{x}^0 \in \mathbb{R}^N$  and  $A \in \mathbb{R}^{M \times N}$  be the unknown original signal and measurement matrix, respectively. Compressed sensing is mathematically formulated as a problem of reconstructing the signal  $\mathbf{x}^0$  from its measurement  $\mathbf{y} = A\mathbf{x}^0$ , where the number of measurements is less than the signal dimension ( $M < N$ ). In general, the problem is underdetermined, and the solution is not unique. However, the signal can be reconstructed utilizing the knowledge that the original signal is sparse; it contains zero components with a finite probability. The reconstruction of signals from a limited number of measurements is a common challenge in various fields. In the past decade, theories and techniques of compressed sensing have been enriched by the interdisciplinary work in the fields such as signal processing, medical imaging, and statistical physics.

A natural way to reconstruct a sparse signal is to minimize the  $\ell_0$  norm under a constraint:

$$\min_{\mathbf{x}} \|\mathbf{x}\|_0, \text{ subject to } \mathbf{y} = A\mathbf{x}, \quad (1)$$

where  $\|\mathbf{x}\|_0$  is the number of nonzero components in  $\mathbf{x}$ . However, a combinatorial search with respect to the support set is required to exactly solve (1); hence, it is unrealistic for implementation. The minimization of  $\ell_1$  norm [1, 3] is a widely used approach:

$$\min_{\mathbf{x}} \|\mathbf{x}\|_1, \text{ subject to } \mathbf{y} = A\mathbf{x}, \quad (2)$$

which is a convex relaxation problem of (1), where  $\|\mathbf{x}\|_1 = \sum_{i=1}^N |x_i|$ . Efficient algorithms to solve (2) have been developed [4, 5], in addition to the convex optimization techniques [6]. Further, the equivalence between the solutions (1) and (2) is mathematically proved when the measurement matrix satisfies the nullspace property and restricted isometry property [7, 8].

Despite the mathematical tractability of  $\ell_1$  minimization, its performance is inferior to  $\ell_0$  minimization for the practical setting of the measurement matrix  $A$ . The difference between  $\ell_1$  and  $\ell_0$  is expected to be reduced by introducing the minimization of  $\ell_p$  ( $0 < p < 1$ ) norm. In fact,  $\ell_p$  ( $0 < p < 1$ ) minimization achieves the reconstruction of the original signal from a fewer number of measurements than  $\ell_1$  minimization [9, 10]. However,  $\ell_p$  ( $0 < p < 1$ ) minimization leads to a discontinuity of the reconstructed signal with respect to the input, which induces algorithmic instability. Smoothly Clipped Absolute Deviation (SCAD) [11] and Minimax Concave Penalty (MCP) [12], which are piecewise continuous nonconvex penalties, are potential candidates to address this limitation. SCAD and MCP are designed to provide continuity, unbiasedness, and sparsity to the estimates, and their nonconvexities are controlled by nonconvexity parameters. The mathematical treatment of nonconvex penalties is seemingly difficult compared with  $\ell_1$ . However, it is shown that a data compression problem under SCAD and MCP can be solved without additional computational cost compared with convex optimization problems in a certain parameter region, and this region is characterized by replica symmetry in the context of statistical physics [13]. This investigation implies prospects of these penalties for improvement in reconstructing the signals in compressed sensing.

In this study, we theoretically verify the performance of the minimization of SCAD and MCP for the reconstruction of sparse signals in compressed sensing. The perfect reconstruction is achieved with a smaller number of measurements compared with  $\ell_1$  reconstruction limit [14, 15, 16]. Further, SCAD and MCP minimization overcomes the algorithmic limit of the Bayes-optimal method [17], by decreasing the values of the nonconvexity parameters. As a reconstruction algorithm, we apply approximate message passing (AMP) to SCAD and MCP minimization. Further, we demonstrate the efficiency of controlling nonconvexity parameters for the perfect reconstruction of rather dense signals. The efficiency of the nonconvexity control is understood by considering the flow and gradient of the state evolution.

The remainder of this paper is organized as follows. In Sec. 2, we introduce the nonconvex sparse penalties, SCAD and MCP, used in this study. The equilibrium properties of compressed sensing under SCAD and MCP are studied in Sec. 3, based on the replica method under replica symmetric (RS) assumption. In Sec. 4, the limit for the perfect reconstruction is derived for SCAD and MCP, and we show that their performance overcomes  $\ell_1$  reconstruction limit and the algorithmic limit of the Bayes-optimal method. In Sec. 5, we demonstrate the actual reconstruction of the signal using AMP in numerical experiments on simulated datasets. Sec. 6 is devoted to the summary and discussion of this paper.

## 2. Definition of SCAD and MCP

The problem considered in this study is formulated as

$$\min_{\mathbf{x}} J(\mathbf{x}; \lambda, a) \text{ subject to } \mathbf{y} = A\mathbf{x}, \quad (3)$$

where  $J(\mathbf{x}; \lambda, a) = \sum_{i=1}^N J(x_i; \lambda, a)$  is a sparsity-inducing penalty and  $\lambda, a$  are regularization parameters. We deal with two types of nonconvex penalties, SCAD and MCP. The shapes of these penalties are controlled by two parameters  $\lambda$  and  $a$ , and  $\ell_1$  penalty is considered as a limit. We call these regularization parameters nonconvexity parameters.

SCAD is defined by [11]

$$J(x; \lambda, a) = \begin{cases} \lambda|x| & (|x| \leq \lambda) \\ -\frac{x^2 - 2a\lambda|x| + \lambda^2}{2(a-1)} & (\lambda < |x| \leq a\lambda) \\ \frac{(a+1)\lambda^2}{2} & (|x| > a\lambda) \end{cases}, \quad (4)$$

where  $\lambda \in (0, \infty)$  and  $a \in (1, \infty)$ . Figure 1 (a) represents SCAD penalty at  $\lambda = 1$  and  $a = 3$ . The dashed vertical lines are the thresholds  $|x| = \lambda$  and  $|x| = a\lambda$ . SCAD penalty for  $|x| \leq \lambda$  is equivalent to  $\ell_1$  penalty, and that for  $|x| > a\lambda$  is equivalent to  $\ell_0$  penalty; i.e., the penalty has a constant value. These  $\ell_1$  and  $\ell_0$  regions are related by a quadratic function. At  $a \rightarrow \infty$ , SCAD is reduced to  $\ell_1$  penalty,  $J(x; \lambda, a \rightarrow \infty) = \lambda|x|$ .

MCP is defined by [12]

$$J(x; \lambda, a) = \begin{cases} \lambda|x| - \frac{x^2}{2a} & (|x| \leq a\lambda) \\ \frac{a\lambda^2}{2} & (|x| > a\lambda) \end{cases}, \quad (5)$$

where  $\lambda \in (0, \infty)$  and  $a \in (1, \infty)$ . Figure 1 (b) represents MCP for  $\lambda = 1$  and  $a = 3$ . The vertical line represents the threshold  $|x| = a\lambda$ . As with SCAD, MCP is also reduced to  $\ell_1$  by taking the limit  $a \rightarrow \infty$ .

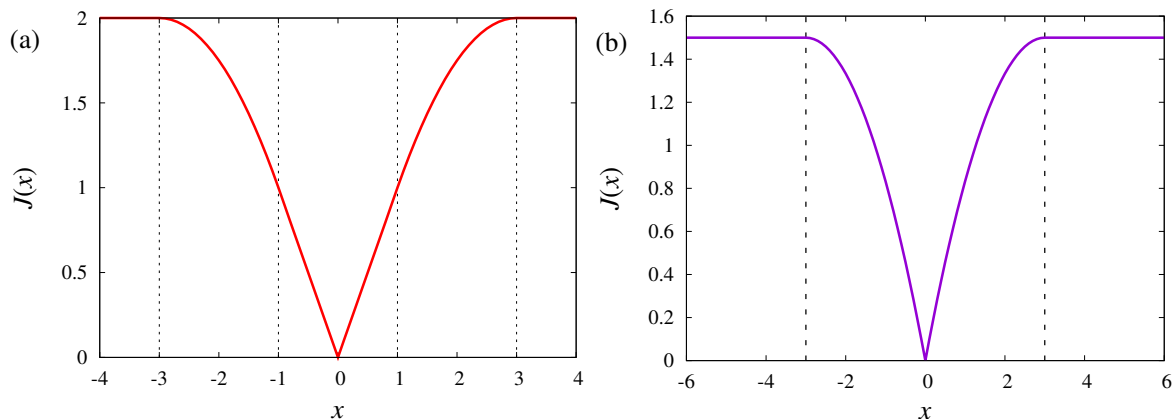


**Figure 1.** Shapes of (a) SCAD for  $\lambda = 1$  and  $a = 3$  and (b) MCP for  $\lambda = 1$  and  $a = 3$ . The dashed lines represent the thresholds where penalty shape changes.

### 3. Replica analysis for SCAD and MCP

We assume that the signal to be reconstructed is generated according to the Bernoulli–Gaussian distribution,

$$P_0(\mathbf{x}^0) = \prod_i \left\{ (1 - \rho)\delta(x_i^0) + \frac{\rho}{\sqrt{2\pi\sigma_x^2}} \exp\left(-\frac{(x_i^0)^2}{2\sigma_x^2}\right) \right\}, \quad (6)$$

where  $\delta(x)$  is the Dirac delta function. Further, we consider the measurement matrix  $A$  to be a random Gaussian, where each component is independently and identically distributed according to the Gaussian distribution with mean 0 and variance  $N^{-1}$ . The measurement is expressed as  $\mathbf{y} = A\mathbf{x}^0$ , and the minimization of  $J(\mathbf{x}; \lambda, a)$  is implemented under the constraint  $\mathbf{y} = A\mathbf{x}$ . For mathematical tractability, we express the constraint  $\mathbf{y} = A\mathbf{x}$  by introducing a parameter  $\tau$  as

$$P_\tau(\mathbf{y}|\mathbf{x}) = \frac{1}{(\sqrt{2\pi\tau})^M} \exp\left\{-\frac{1}{2\tau}\|\mathbf{y} - A\mathbf{x}\|_2^2\right\}, \quad (7)$$

where the probability is concentrated at  $\mathbf{y} = A\mathbf{x}$  taking the limit  $\tau \rightarrow 0$ . The posterior distribution corresponding to the problem (3) is given by

$$P_\beta(\mathbf{x}|\mathbf{y}) = \lim_{\tau \rightarrow 0} \frac{1}{Z_{\beta,\tau}(\mathbf{y})} \exp(-\beta J(\mathbf{x}; \lambda, a)) P_\tau(\mathbf{y}|\mathbf{x}), \quad (8)$$

which converges to the uniform distribution over the minimizer of (3) at  $\beta \rightarrow \infty$ , and

$$Z_{\beta,\tau}(\mathbf{y}) = \int d\mathbf{x} \exp(-\beta J(\mathbf{x}; \lambda, a)) P_\tau(\mathbf{y}|\mathbf{x}) \quad (9)$$

is the normalization constant. The point estimate of the minimizer of (3) is given by  $\hat{\mathbf{x}} = \lim_{\beta \rightarrow \infty} \langle \mathbf{x} \rangle$ , where  $\langle \cdot \rangle$  denotes the expectation with respect to  $\mathbf{x}$  according to the posterior distribution (8).

We examine the typical performance of the SCAD and MCP minimization at  $N \rightarrow \infty$  and  $M \rightarrow \infty$  keeping  $M/N = \alpha \sim O(1)$ , where  $\alpha$  is the compression ratio.

Free energy density defined by

$$f = - \lim_{\beta \rightarrow \infty} \lim_{N \rightarrow \infty} \lim_{\tau \rightarrow 0} \frac{1}{N\beta} E_{\mathbf{x}^0, A}[\ln Z_{\beta, \tau}(\mathbf{y})] \quad (10)$$

is the key in this discussion, where  $E_{\mathbf{x}^0, A}[\cdot \cdot \cdot]$  denotes the expectation with respect to  $A$  and  $\mathbf{x}^0$ . It is calculated using the following identity

$$E_{\mathbf{x}^0, A}[\ln Z_{\beta, \tau}(\mathbf{y})] = \lim_{n \rightarrow 0} \frac{E_{\mathbf{x}^0, A}[Z_{\beta, \tau}^n(\mathbf{y})] - 1}{n}. \quad (11)$$

Assuming that  $n$  is an integer, we can express the expectation of  $Z_{\beta}^n$  in (11) using  $n$ -replicated systems

$$\begin{aligned} E_{\mathbf{x}^0, A}[Z_{\beta, \tau}^n(\mathbf{y})] &= \int dA d\mathbf{y} d\mathbf{x}^0 P_0(\mathbf{x}^0) P_A(A) \delta(\mathbf{y} - A\mathbf{x}^0) \\ &\times \int d\mathbf{x}^{(1)} \dots d\mathbf{x}^{(n)} \lim_{\tau \rightarrow 0} \frac{1}{(\sqrt{2\pi\tau})^{nM}} \\ &\times \exp \left[ \sum_{a=1}^n \left\{ -\frac{1}{2\tau} \|\mathbf{y} - A\mathbf{x}^{(a)}\|_2^2 - \beta J(\mathbf{x}^{(a)}; \lambda, a) \right\} \right]. \end{aligned} \quad (12)$$

Following the calculations shown in [13, 16], the free energy density under the RS assumption is given by

$$f = \text{extr}_{\Omega, \tilde{\Omega}} \left[ \frac{\alpha(Q - 2m + \rho\sigma_x^2)}{2\chi} + m\tilde{m} - \frac{\tilde{Q}Q - \tilde{\chi}\chi}{2} + \frac{\xi(\tilde{Q}, \sigma)}{2} \right], \quad (13)$$

where  $\text{extr}_{\Omega, \tilde{\Omega}}$  represents the extremization with respect to the quantities  $\Omega = \{Q, \chi, m\}$  and  $\tilde{\Omega} = \{\tilde{Q}, \tilde{\chi}, \tilde{m}\}$ . The function  $\xi(\tilde{Q}, \sigma)$  depends on the regularization as

$$\xi(\tilde{Q}, \sigma) = 2 \int Dz L(\tilde{Q}, \sigma z), \quad (14)$$

$$L(\tilde{Q}, \sigma z) = \min_x \left( \frac{\tilde{Q}}{2} x^2 - \sigma z x + J(x; \lambda, a) \right), \quad (15)$$

where  $\int Dz = \int_{-\infty}^{\infty} dz \exp(-z^2/2)/\sqrt{2\pi}$ . The parameter  $\sigma z$  is a random field that effectively represents the randomness induced by  $\mathbf{x}^0$  and  $A$ , and  $\overline{\cdot \cdot \cdot}$  denotes the average over  $\sigma$  according to the distribution

$$P_{\sigma}(\sigma) = (1 - \rho)\delta(\sigma - \sigma_-) + \rho\delta(\sigma - \sigma_+), \quad (16)$$

with  $\sigma_- = \sqrt{\tilde{\chi}}$  and  $\sigma_+ = \sqrt{\tilde{\chi} + \tilde{m}^2\sigma_x^2}$ . We denote the solution of  $x$  in the effective single-body problem (15) as  $x^*(\tilde{Q}^{-1}, \sigma z)$ , which depends on the regularization. The saddle point equations are given by

$$\chi = - \frac{\overline{\partial \xi(\tilde{Q}, \sigma)}}{\partial \tilde{\chi}} = \int Dz \frac{\overline{\partial x^*(\tilde{Q}^{-1}, \sigma z)}}{\partial(\sigma z)}, \quad (17)$$

$$Q = \frac{\overline{\partial \xi(\tilde{Q}, \sigma)}}{\partial \tilde{Q}} = \int Dz \overline{(x^*(\tilde{Q}^{-1}, \sigma z))^2}, \quad (18)$$

$$m = -\frac{1}{2} \frac{\overline{\partial \xi(\tilde{Q}, \sigma)}}{\partial \tilde{m}} = \rho \tilde{m} \sigma_x^2 \int Dz \frac{\overline{\partial x^*(\tilde{Q}^{-1}, \sigma_+ z)}}{\partial(\sigma_+ z)}, \quad (19)$$

$$\tilde{\chi} = \frac{\alpha(Q - 2m + \rho\sigma_x^2)}{\chi^2}, \quad (20)$$

$$\tilde{Q} = \frac{\alpha}{\chi}, \quad (21)$$

$$\tilde{m} = \frac{\alpha}{\chi}. \quad (22)$$

At the saddle point,  $x^*(\tilde{Q}^{-1}, \sigma z)$  is statistically equivalent to the point estimate  $\hat{\mathbf{x}}$ , and  $\chi, Q$  and  $m$  are related to the physical quantities as

$$Q = \lim_{N \rightarrow \infty} \frac{1}{N} \sum_{i=1}^N E_{\mathbf{x}^0, A}[\hat{x}_i^2], \quad (23)$$

$$m = \lim_{N \rightarrow \infty} \frac{1}{N} \sum_{i=1}^N E_{\mathbf{x}^0, A}[x_i^0 \hat{x}_i], \quad (24)$$

$$\chi = \lim_{\beta \rightarrow \infty} \lim_{N \rightarrow \infty} \frac{\beta}{N} \sum_{i=1}^N E_{\mathbf{x}^0, A}[\langle x_i^2 \rangle - \langle x_i \rangle^2]. \quad (25)$$

Hence, the expectation value of the mean squared error between the reconstructed signal and the original signal is represented as

$$\varepsilon \equiv \frac{1}{N} E_{\mathbf{x}^0, A} [\|\hat{\mathbf{x}} - \mathbf{x}^0\|_2^2] = Q - 2m + \rho\sigma_x^2. \quad (26)$$

The saddle point equations for variables  $\Omega = \{Q, \chi, m\}$  directly depend on the functional form of the regularization, but the equations for  $\tilde{\Omega}$  do not depend on it. In the following subsections, we show the form of saddle point equations of  $\Omega$  for SCAD and MCP.

The RS solution is stable against the symmetry breaking perturbation when [13, 16]

$$\frac{\alpha}{\chi^2} \int Dz \overline{\left( \frac{\partial x^*(\tilde{Q}^{-1}, \sigma z)}{\partial(\sigma z)} \right)^2} < 1, \quad (27)$$

which is known as de Almeida–Thouless (AT) condition [18]. The form of this condition also depends on the functional form of the regularization.

### 3.1. SCAD

For considering the solution of the single-body problem (15) for SCAD, we have to consider the range of  $a$ , because SCAD penalty has a quadratic term as shown in (4). To obtain the finite minimizer of (15),  $\tilde{Q} > (a - 1)^{-1}$  should hold. Along with the restriction of  $a$  that appears in the SCAD's definition,  $a$  should be  $a \in (a_{\min}, \infty)$ , where

$$a_{\min} = \max \left\{ 1, 1 + \frac{\chi}{\alpha} \right\}, \quad (28)$$

and we immediately obtain  $a_{\min} = 1 + \chi/\alpha$  because  $\chi \geq 0$ . When  $a \in (a_{\min}, \infty)$ , the minimizer of (15) under SCAD is given by [19]

$$x^*(\tilde{Q}^{-1}, \sigma z) = \Sigma_{\text{SCAD}}(\tilde{Q}^{-1}, \sigma z) \mathcal{M}_{\text{SCAD}}(\tilde{Q}^{-1}, \sigma z), \quad (29)$$

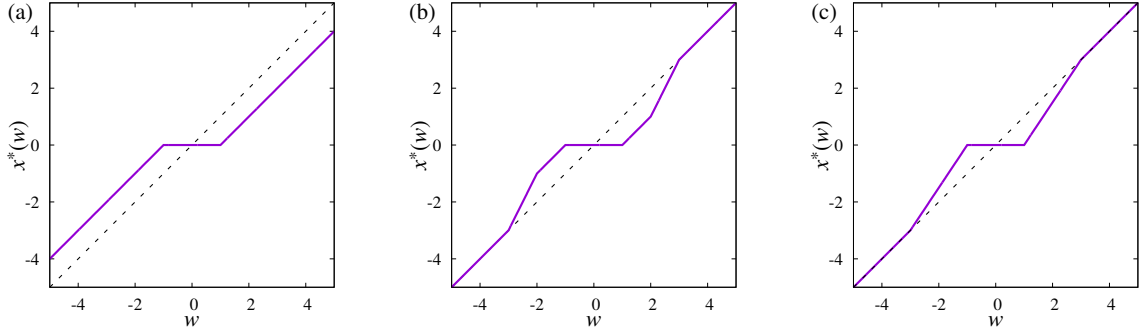


**Figure 2.** Behaviour of the estimator for (a)  $\ell_1$ , (b) SCAD, and (c) MCP. The dashed diagonal lines represent OLS estimator.

where

$$\mathcal{M}_{\text{SCAD}}(s, w) = \begin{cases} w - \text{sgn}(w)\lambda & \text{for } \lambda(1 + s^{-1}) \geq |w| > \lambda \\ w - \text{sgn}(w)\frac{a\lambda}{a-1} & \text{for } a\lambda s^{-1} \geq |w| > \lambda(1 + s^{-1}) \\ w & \text{for } |w| > a\lambda s^{-1} \\ 0 & \text{otherwise} \end{cases}, \quad (30)$$

$$\Sigma_{\text{SCAD}}(s, w) = \begin{cases} s & \text{for } \lambda(1 + s^{-1}) \geq |w| > \lambda \\ (s^{-1} - \frac{1}{a-1})^{-1} & \text{for } a\lambda s^{-1} \geq |w| > \lambda(1 + s^{-1}) \\ s & \text{for } |w| > a\lambda s^{-1} \\ 0 & \text{otherwise} \end{cases}, \quad (31)$$

and  $\text{sgn}(w)$  denotes the sign of  $w$ . An example of the estimator under SCAD is shown in Figure 2 (b). The SCAD estimator behaves like the  $\ell_1$  estimator, which is shown in Figure 2 (a), and like the ordinary least square (OLS) estimator when  $\lambda(1 + s^{-1}) \geq |z| > \lambda$  and  $|w| > a\lambda s^{-1}$ , respectively. In the region  $a\lambda s^{-1} \geq |w| > \lambda(1 + s^{-1})$ , the estimator linearly transits between  $\ell_1$  and OLS estimators.

Substituting the solution (29) into (15), we obtain

$$-2L(\tilde{Q}, \sigma z) = \begin{cases} \frac{(\sigma z - \lambda \text{sgn}(z))^2}{\tilde{Q}} & (\sqrt{2}\theta_1(\sigma) < |z| \leq \sqrt{2}\theta_2(\sigma)) \\ \frac{(\sigma z - \frac{a\lambda}{a-1})^2}{\tilde{Q} - \frac{1}{a-1}} + \frac{\lambda^2}{a-1} & (\sqrt{2}\theta_2(\sigma) < |z| \leq \sqrt{2}\theta_3(\sigma)) \\ \frac{(\sigma z)^2}{\tilde{Q}} - (a+1)\lambda^2 & (|z| > \sqrt{2}\theta_3(\sigma)) \\ 0 & (\text{otherwise}) \end{cases}, \quad (32)$$

where  $\theta_1(\sigma) = \lambda/(\sqrt{2}\sigma)$ ,  $\theta_2(\sigma) = \lambda(1 + \tilde{Q})/(\sqrt{2}\sigma)$ , and  $\theta_3(\sigma) = a\lambda\tilde{Q}/(\sqrt{2}\sigma)$ . Equation (14) for SCAD regularization is derived as

$$-\xi(\sigma) = \xi_1(\sigma) + \xi_2(\sigma) + \xi_3(\sigma) + \frac{\lambda^2 \xi_4(\sigma)}{a-1} - (a+1)\lambda^2 \text{erfc}(\theta_3(\sigma)), \quad (33)$$

where

$$\xi_1(\sigma) = \frac{\sigma^2}{\tilde{Q}} \left[ -\frac{2\theta_1(\sigma)}{\sqrt{\pi}} \left( e^{-\theta_1^2(\sigma)} + (\tilde{Q} - 1)e^{-\theta_2^2(\sigma)} \right) \right]$$

$$+ (1 + 2\theta_1^2(\sigma))\{\operatorname{erfc}(\theta_1(\sigma)) - \operatorname{erfc}(\theta_2(\sigma))\}], \quad (34)$$

$$\begin{aligned} \xi_2(\sigma) &= \frac{\sigma^2}{\tilde{Q} - \frac{1}{a-1}} \left[ \frac{2}{\sqrt{\pi}} \left\{ \theta_2(\sigma) e^{-\theta_2^2(\sigma)} \right. \right. \\ &\quad \left. \left. - \theta_3(\sigma) e^{-\theta_3^2(\sigma)} - \frac{2\theta_3(\sigma)}{\tilde{Q}(a-1)} \left( e^{-\theta_2^2(\sigma)} - e^{-\theta_3^2(\sigma)} \right) \right\} \right. \\ &\quad \left. + \left\{ 1 + 2 \left( \frac{\theta_3(\sigma)}{\tilde{Q}(a-1)} \right)^2 \right\} \xi_4(\sigma) \right], \end{aligned} \quad (35)$$

$$\xi_3(\sigma) = \frac{\sigma^2}{\tilde{Q}} \left[ \frac{2\theta_3(\sigma)}{\sqrt{\pi}} e^{-\theta_3^2(\sigma)} + \operatorname{erfc}(\theta_3(\sigma)) \right], \quad (36)$$

$$\xi_4(\sigma) = \operatorname{erfc}(\theta_2(\sigma)) - \operatorname{erfc}(\theta_3(\sigma)). \quad (37)$$

The regularization-dependent saddle point equations are given by

$$Q = \frac{\xi_1(\sigma)}{\tilde{Q}} + \frac{\xi_2(\sigma)}{\tilde{Q} - \frac{1}{a-1}} + \frac{\xi_3(\sigma)}{\tilde{Q}}, \quad (38)$$

$$\chi = \frac{1}{\tilde{Q}} \left[ \hat{\rho} + \frac{1}{\tilde{Q} - \frac{1}{a-1}} \overline{\xi_4(\sigma)} \right], \quad (39)$$

$$m = \rho \sigma_x^2 \left[ \operatorname{erfc}(\theta_1(\sigma_+)) + \frac{1}{\tilde{Q} - \frac{1}{a-1}} \overline{\xi_4(\sigma_+)} \right], \quad (40)$$

where  $\hat{\rho}$  is the density of the nonzero component in the estimate given by

$$\hat{\rho} = \overline{\operatorname{erfc}(\theta_1(\sigma))}. \quad (41)$$

From (27), the AT condition is derived as

$$\frac{1}{\alpha} \left[ \hat{\rho} + \left\{ \left( \frac{\tilde{Q}}{\tilde{Q} - \frac{1}{a-1}} \right)^2 - 1 \right\} \overline{\xi_4(\sigma)} \right] < 1. \quad (42)$$

### 3.2. MCP

From the same argument as SCAD, when  $a \in (a_{\min}, \infty)$ , where

$$a_{\min} = \max\{1, \chi/\alpha\}, \quad (43)$$

the solution of the single body problem under MCP is given by [19]

$$x^*(\tilde{Q}^{-1}, \sigma z) = \Sigma_{\text{MCP}}(\tilde{Q}^{-1}, \sigma z) \mathcal{M}_{\text{MCP}}(\tilde{Q}^{-1}, \sigma z), \quad (44)$$

where

$$\mathcal{M}_{\text{MCP}}(s, w) = \begin{cases} w - \operatorname{sgn}(w)\lambda & \text{for } a\lambda s^{-1} \geq |w| > \lambda \\ w & \text{for } |w| > a\lambda s^{-1} \\ 0 & \text{otherwise} \end{cases}, \quad (45)$$

$$\Sigma_{\text{MCP}}(s, w) = \begin{cases} (s^{-1} - a^{-1})^{-1} & \text{for } a\lambda s^{-1} \geq |w| > \lambda \\ s & \text{for } |w| > a\lambda s^{-1} \\ 0 & \text{otherwise} \end{cases}. \quad (46)$$



Figure 2 (c) shows the behaviour of the MCP estimator. The MCP estimator behaves like the OLS estimator at  $|w| > a\lambda s^{-1}$ , and is connected from zero to the OLS estimator in the region  $a\lambda s^{-1} \geq |w| > \lambda$ . We obtain

$$-2L(\tilde{Q}, \sigma) = \begin{cases} \frac{(\sigma z - \lambda \text{sgn}(z))^2}{\tilde{Q} - a^{-1}} & (\sqrt{2}\theta_1(\sigma) < |z| \leq \sqrt{2}\theta_2(\sigma)) \\ \frac{(\sigma z)^2}{\tilde{Q}} - \lambda a^2 & (|z| > \sqrt{2}\theta_2(\sigma)) \\ 0 & (\text{otherwise}) \end{cases}, \quad (47)$$

where  $\theta_1(\sigma) = \lambda/(\sqrt{2}\sigma)$  and  $\theta_2(\sigma) = a\lambda\tilde{Q}/(\sqrt{2}\sigma)$ , and (14) for MCP is derived as

$$-\xi(\sigma) = \xi_1(\sigma) + \xi_2(\sigma), \quad (48)$$

where

$$\xi_1(\sigma) = -\frac{2\sigma^2}{\sqrt{\pi}(\tilde{Q} - a^{-1})} \left\{ \theta_1(\sigma)(e^{-\theta_1^2(\sigma)} - e^{-\theta_2^2(\sigma)}) - e^{-\theta_2^2(\sigma)}(\theta_1(\sigma) - \theta_2(\sigma)) \right\} + \frac{(\sigma^2 + \lambda^2)\xi_3(\sigma)}{\tilde{Q} - a^{-1}}, \quad (49)$$

$$\xi_2(\sigma) = \frac{\sigma^2}{\tilde{Q}} \left( \frac{2\theta_2(\sigma)}{\sqrt{\pi}} e^{-\theta_2^2(\sigma)} + \text{erfc}(\theta_2(\sigma)) \right) - \lambda a^2 \text{erfc}(\theta_2(\sigma)), \quad (50)$$

$$\xi_3(\sigma) = \text{erfc}(\theta_1(\sigma)) - \text{erfc}(\theta_2(\sigma)). \quad (51)$$

The saddle point equations for  $\Omega$  are given by

$$Q = \frac{\xi_1(\sigma)}{\tilde{Q} - \frac{1}{a}} + \frac{\sigma^2}{\tilde{Q}^2} \left\{ \frac{2\theta_2(\sigma)}{\sqrt{\pi}} e^{-\theta_2^2(\sigma)} + \text{erfc}(\theta_2(\sigma)) \right\}, \quad (52)$$

$$\chi = \frac{1}{\tilde{Q}} \left[ \hat{\rho} + \frac{a^{-1}\xi_3(\sigma)}{\tilde{Q} - a^{-1}} \right], \quad (53)$$

$$m = \rho\sigma_x^2 \left[ \text{erfc}(\theta_1(\sigma_+)) + \frac{a^{-1}\xi_3(\sigma_+)}{\tilde{Q} - a^{-1}} \right], \quad (54)$$

where  $\hat{\rho}$  is the density of nonzero component in the estimate given by

$$\hat{\rho} = \overline{\text{erfc}(\theta_1(\sigma))}. \quad (55)$$

The AT condition for MCP is derived as

$$\frac{1}{\alpha} \left[ \hat{\rho} + \left\{ \left( \frac{\tilde{Q}}{\tilde{Q} - a^{-1}} \right)^2 - 1 \right\} \overline{\xi_3(\sigma)} \right] < 1. \quad (56)$$

#### 4. Stability of success solution

One of the solutions of the saddle point equations is characterized by  $Q = m = \rho\sigma_x^2$ . Following the correspondence between the order parameters and the MSE (26), this solution indicates the perfect reconstruction of the original signal  $\mathbf{x}^0$ . Hence, we call the solution with  $Q = m = \rho\sigma_x^2$  the *success solution*. The saddle point equation can

have solutions other than the success solution; however, these solutions do not satisfy the AT condition as far as we observed. Substituting the relationship  $Q = m = \rho\sigma_x^2$ , we immediately obtain  $\chi = 0$  and  $\tilde{Q} = \tilde{m} = \infty$ , and the only variable to be solved is  $\tilde{\chi}$ . The expansion of  $Q$  and  $m$  up to the order  $O(\tilde{Q}^{-2})$  gives the expression of  $\tilde{\chi}$  for the success solution under SCAD

$$\begin{aligned} \tilde{\chi} = & \frac{1-\rho}{\alpha} \left[ -\frac{2\tilde{\chi}}{\sqrt{\pi}}\theta_- e^{-\theta_-^2} + (\tilde{\chi} + \lambda^2)\text{erfc}(\theta_-) \right] \\ & + \frac{\rho}{\alpha} \left[ \tilde{\chi} + \lambda^2 \{1 - \text{erfc}(\theta_+)\} + \left\{ \left( \frac{a\lambda}{a-1} \right)^2 + \frac{\sigma_x^2}{(a-1)^2} \right\} \{\text{erfc}(\theta_+) - \text{erfc}(a\theta_+)\} \right. \\ & \left. + \frac{2\sigma_x^2\theta_+}{\sqrt{\pi}(a-1)} \left\{ \frac{a}{a-1}(e^{-a^2\theta_+^2} - e^{-\theta_+^2}) - e^{-\theta_+^2} \right\} \right], \end{aligned} \quad (57)$$

and under MCP

$$\begin{aligned} \tilde{\chi} = & \frac{1-\rho}{\alpha} \left\{ -\frac{2\tilde{\chi}}{\sqrt{\pi}}\theta_- e^{-\theta_-^2} + (\tilde{\chi} + \lambda^2)\text{erfc}(\theta_-) \right\} \\ & + \frac{\rho}{\alpha} \left[ \tilde{\chi} + \left( \lambda^2 + \frac{\sigma_x^2}{a^2} \right) (1 - \text{erfc}(a\theta_+)) + \frac{2\sigma_x^2\theta_+}{a\sqrt{\pi}} e^{-a^2\theta_+^2} - \frac{4\sigma_x^2\theta_+}{a\sqrt{\pi}} \right], \end{aligned} \quad (58)$$

where  $\theta_- = \lambda/\sqrt{2\tilde{\chi}}$  and  $\theta_+ = \lambda/\sqrt{2\sigma_x^2}$ . Eqs. (57) and (58) are reduced to the saddle point equation of  $\tilde{\chi}$  corresponding to the success solution for  $\ell_1$  regularization by setting  $\lambda = 1$  and when  $a \rightarrow \infty$  [16].

For both the penalties, the success solution is a locally stable solution as a saddle point of the RS free energy when

$$\frac{1}{\alpha} \{(1-\rho)\text{erfc}(\theta_-) + \rho\} < 1. \quad (59)$$

This condition is derived by the linear stability analysis of  $\chi$  around 0. Further, we can show that the AT condition for the success solution is equivalent to (59). This means that when the success solution is locally stable as a RS saddle point, it is also stable with respect to the replica symmetry breaking perturbation. Therefore, the reconstruction limit  $\alpha_c(\rho)$  is defined as the minimum value of  $\alpha$  that satisfies (59) for each  $\rho$ .

Figs. 3 and 4 show the  $\rho$ -dependence of  $\alpha_c(\rho)$  for SCAD minimization and MCP minimization, respectively, where (a)s represent  $a = 3$  and (b)s represent  $\lambda = 0.01$ . The typical reconstruction is possible in the parameter region  $\alpha \geq \alpha_c(\rho)$ , and that for  $\ell_1$  minimization (L1) and the algorithmic limit of the Bayes-optimal method (BO) are shown for comparison. As  $\lambda$  and  $a$  decrease,  $\alpha_c(\rho)$  of SCAD and MCP become less than that of the algorithmic limit of the Bayes-optimal reconstruction method [17]. Further, the reconstruction limit  $\alpha_c(\rho)$  approaches  $\rho$  as  $\lambda \rightarrow 0$ . Mathematically,  $\alpha_c(\rho) \rightarrow \rho$  is provided by scaling  $\theta_- \rightarrow \infty$  and  $\tilde{\chi} \rightarrow 0$  at  $\lambda \rightarrow 0$ , which reduces (59) to  $\rho < \alpha$ . This inequality,  $\rho < \alpha$ , is considered to be the principle limit, because in general sparse estimation methods, the estimation of the support increases the effective degrees of the estimated variables. Hence, we need more measurements than the number of the variables to be estimated. It is indicated that SCAD and MCP with  $\lambda \rightarrow 0$  achieve

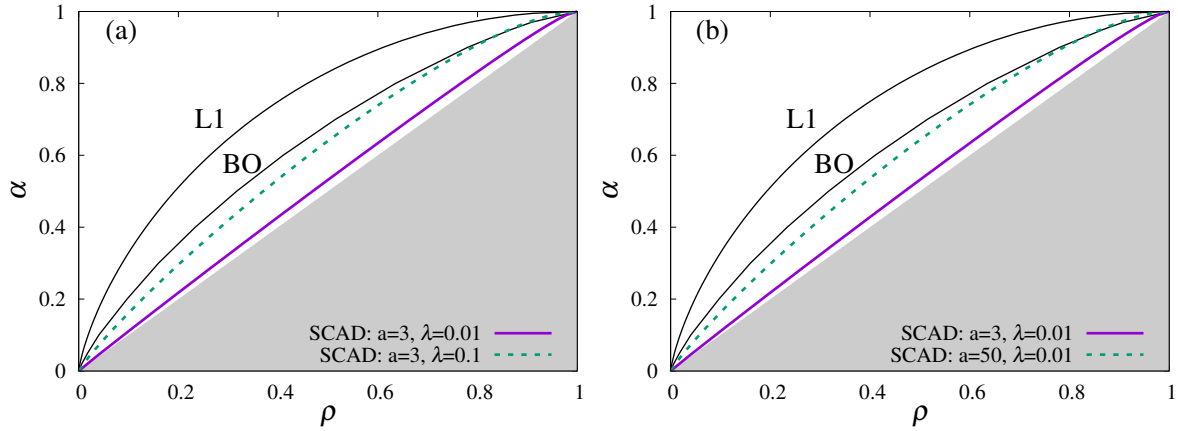


**Figure 3.** Reconstruction limit of SCAD at (a)  $a = 3$  for  $\lambda = 0.01$  and  $\lambda = 0.1$  and (b)  $\lambda = 0.01$   $a = 3$  and  $a = 50$ . The lines with ‘L1’ and ‘BO’ are the reconstruction limit under  $\ell_1$  minimization and the algorithmic limit by the Bayes-optimal method, respectively. The shaded regions are  $\alpha < \rho$ .

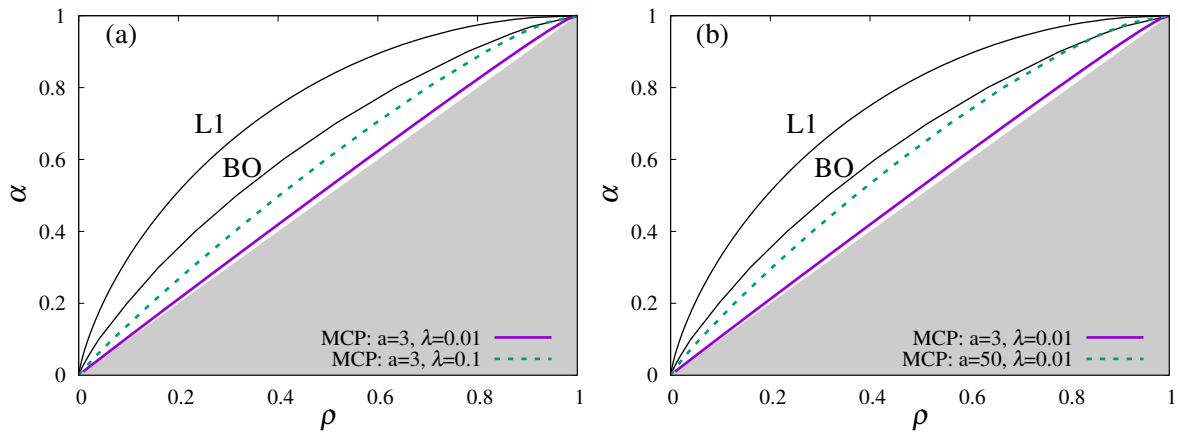


**Figure 4.** Reconstruction limit of MCP at (a)  $a = 3$  for  $\lambda = 0.01$  and  $\lambda = 0.1$  and (b)  $\lambda = 0.01$  for  $a = 3$  and  $a = 50$ . The lines with ‘L1’ and ‘BO’ are the reconstruction limit under  $\ell_1$  minimization and the algorithmic limit by the Bayes-optimal method, respectively. The shaded regions are  $\alpha < \rho$ .

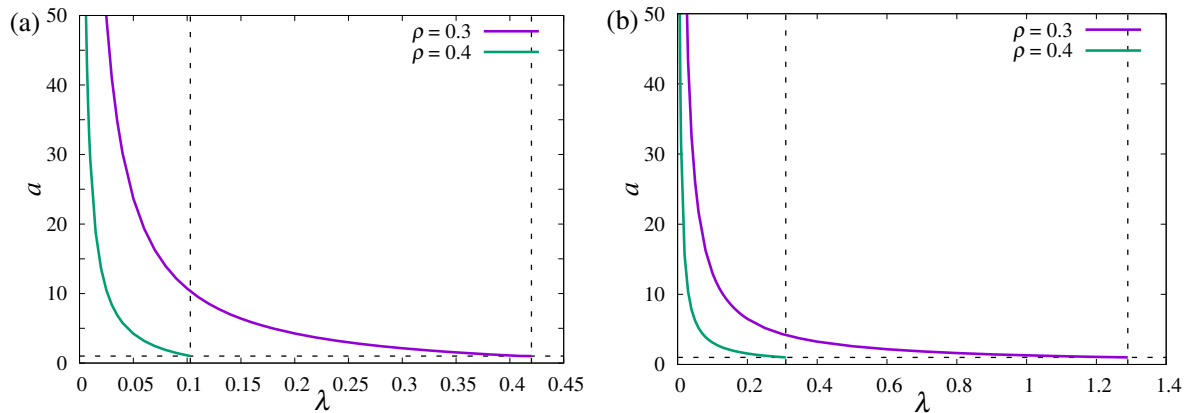


**Figure 5.** Reconstruction limit  $a_c(\lambda)$  at  $\alpha = 0.5$  for (a) SCAD and (b) MCP, respectively. The vertical dashed lines represent the maximum value of  $\lambda$ , where the reconstruction is possible with  $a_{\min} < a \leq a_c(\lambda)$ . The horizontal dashed lines represent  $a = 1$ , which is the minimum value of  $a$  for the success solution.

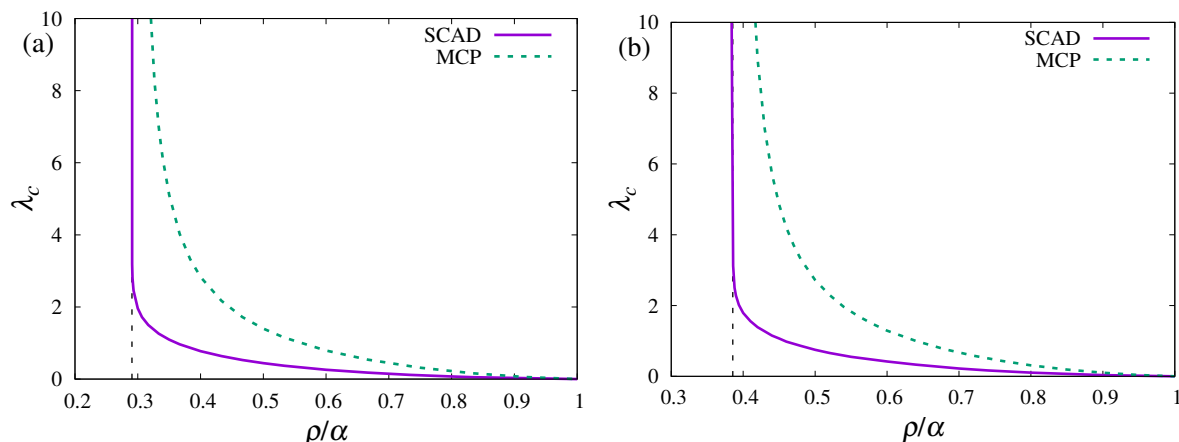


**Figure 6.**  $\rho/\alpha$ -dependence of  $\lambda_c$  for (a)  $\alpha = 0.3$  and (b)  $\alpha = 0.5$ . In the parameter region on the left side to the vertical lines,  $\ell_1$  minimization reconstructs the original signals.

the typical reconstruction when the number of the measurements and that of nonzero variables are balanced.

We denote the value of  $a$  under which the signals can be reconstructed as  $a_c(\lambda)$  for each  $\lambda$ . The reconstruction limit  $a_c(\lambda)$  on the  $\lambda - a$  plane is shown in Figure 5 for (a) SCAD and (b) MCP, respectively, at  $\alpha = 0.5$  for  $\rho = 0.3$  and  $\rho = 0.4$ . The horizontal dashed lines represent  $a_{\min}$ , which is equal to 1 when the success solution is stable, and the signals can be reconstructed in the parameter region  $a_{\min} < a \leq a_c(\lambda)$ . The dashed vertical lines represent  $\lambda_c$ , defined as the maximum value of  $\lambda$  that gives  $a_c(\lambda) > a_{\min}$ . Hence, the signal cannot be reconstructed at  $\lambda \geq \lambda_c$ . For the reconstruction of dense signals, small nonconvexity parameters  $\lambda$  and  $a$  are required, and  $a_c(\lambda)$  and  $\lambda_c$  for MCP are always greater than for SCAD. The dependence of  $\lambda_c$  on  $\rho/\alpha$  for SCAD and MCP are compared in Figure 6 for (a)  $\alpha = 0.3$  and (b)  $\alpha = 0.5$ . The vertical lines represent the reconstruction limit of  $\ell_1$  minimization, and the values of  $\lambda_c$  diverge as  $\rho/\alpha$  approaches the  $\ell_1$  reconstruction limit. This divergence of  $\lambda_c$  means that one can reconstruct the signals using any  $\lambda \in (0, \infty)$  and  $a \in (a_{\min}, \infty)$  when the signals are sufficiently sparse to be reconstructed by  $\ell_1$  minimization. For any system parameters, the divergence of  $\lambda_c$  in MCP is faster than that in SCAD, which indicates that the possible values of nonconvexity parameters for reconstruction in MCP are greater than that in SCAD. In this sense, MCP is superior to SCAD, which is one of the outcomes of this study.

We mention the existence of the solution of RS saddle point equation at  $\alpha < \alpha_c$  for subsequent discussions. One can find a solution with  $\varepsilon > 0$  ( $Q < \rho\sigma_x^2$  and  $m < \rho\sigma_x^2$ ) and  $\chi > 0$ , which is termed as the *failure solution*, at  $\alpha < \alpha_c$ . Figs. 7 and 8 show  $\alpha$ -dependence of  $\varepsilon$  and  $\chi$  for SCAD and MCP, respectively, where the vertical dashed lines represent  $\alpha_c$ . The failure solution always violates the AT condition. Hence, it does not contribute to the equilibrium property of the system for any  $\alpha (< \alpha_c)$ , and is smoothly connected to the success solution that appears  $\alpha \geq \alpha_c$ . As the values of the nonconvexity parameters decrease, the values of  $\varepsilon$  and  $\chi$  diverge at sufficiently small  $\alpha$ ,

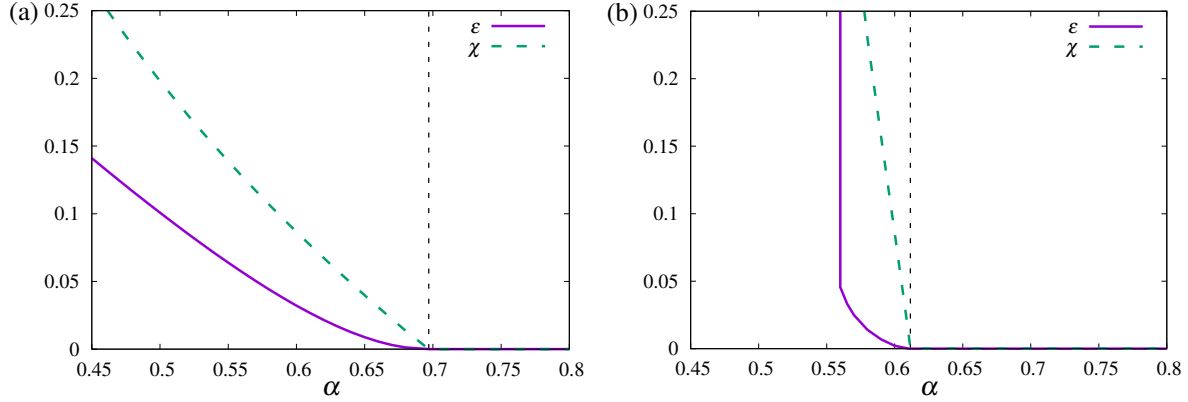


**Figure 7.**  $\alpha$ -dependence of  $\varepsilon$  and  $\chi$  in RS solution of SCAD at  $\rho = 0.35$  for (a)  $\lambda = 1, a = 10$  and (b)  $\lambda = 0.3, a = 5$ . The vertical dashed lines indicate  $\alpha_c$ .

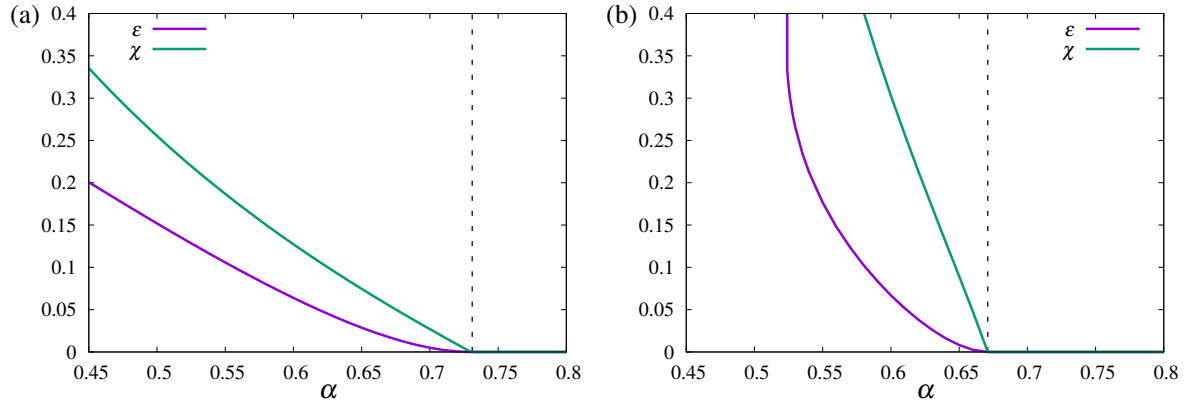


**Figure 8.**  $\alpha$ -dependence of  $\varepsilon$  and  $\chi$  in RS solution of MCP at  $\rho = 0.4$  for (a)  $\lambda = 1, a = 10$  and (b)  $\lambda = 0.5, a = 5$ . The vertical dashed lines indicate  $\alpha_c$ .

and the solution with finite  $\varepsilon$  and  $\chi$  disappears.

## 5. Approximate message passing with nonconvexity control

For numerical computation of the estimate under a given measurement matrix, AMP is a feasible algorithm with low computational cost. In AMP, the estimates under a general separable sparse penalty is recursively updated as

$$\hat{x}_i^{(t+1)} = \arg \min_x \left\{ \frac{\tilde{Q}_i^{(t)}}{2} x^2 - h_i^{(t)} x + J(x_i; \lambda, a) \right\}, \quad (60)$$

where  $\hat{x}_i^{(t)}$  denotes the estimate at time step  $t$ , and

$$\tilde{Q}_i^{(t)} = \sum_{\mu=1}^M \frac{A_{\mu i}^2}{\hat{V}_\mu^{(t)}}, \quad (61)$$

$$h_i^{(t)} = \hat{x}_i^{(t-1)} \tilde{Q}_i^{(t)} + \sum_{\mu=1}^M A_{\mu i} R_\mu^{(t)}, \quad (62)$$

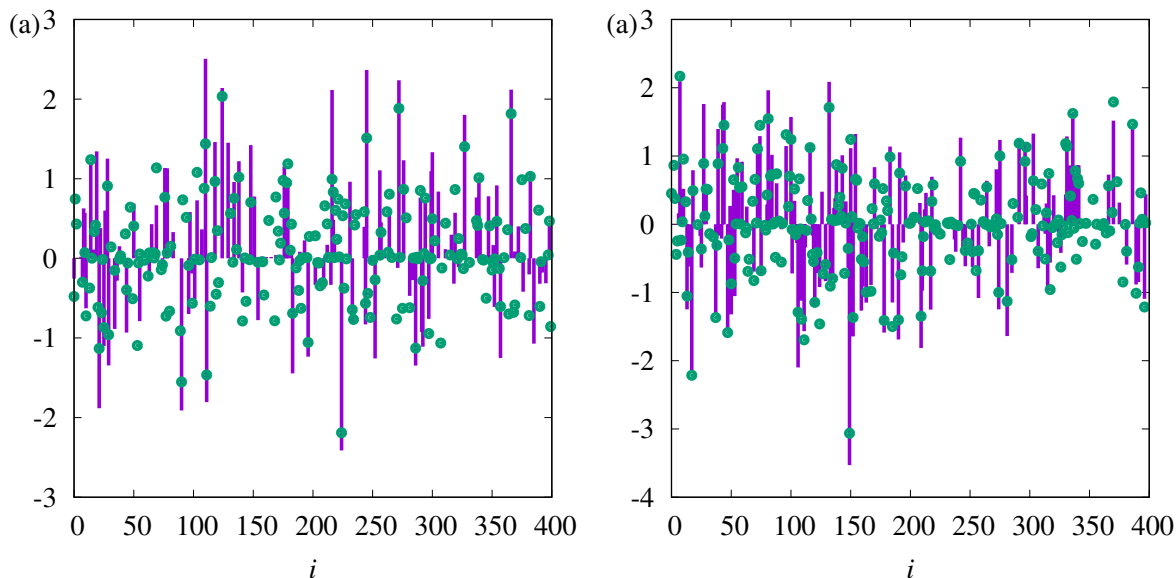


**Figure 9.** Reconstructed signal (circles) under  $\lambda = 0.1$  and  $a = 3$  after 20000 iterations of AMP for (a) SCAD at  $\alpha = 0.5, \rho = 0.35, N = 400$  and (b) MCP at  $\alpha = 0.5, \rho = 0.4, N = 400$ . The original signal is represented by solid lines.

$$\hat{V}_\mu^{(t)} = \sum_{i=1}^N A_{\mu i}^2 \hat{v}_i^{(t-1)}, \quad (63)$$

$$\hat{v}_i^{(t)} = \frac{\partial \hat{x}_i^{(t)}}{\partial h_i^{(t)}}, \quad (64)$$

$$R_\mu^{(t)} = \frac{y_\mu - \sum_i A_{\mu i} \hat{x}_i^{(t-1)}}{\hat{V}_\mu^{(t)}}. \quad (65)$$

The solution of (60) is equivalent to the minimizer of (15), with the replacement of  $\tilde{Q}$  and  $\sigma z$  with  $\tilde{Q}_i^{(t)}$  and  $h_i^{(t)}$ , respectively.

The local stability of AMP corresponds to the AT instability condition [13]. Hence, it is expected that AMP reconstructs the original signal in the theoretically derived parameter region  $\alpha > \alpha_c(\rho)$  at sufficiently large  $N$ , because the current problem does not exhibit any first order transitions in contrast to the Bayes-optimal setting [17] or the Monte Carlo sampling case [20]. Figure 9 is an example of reconstructed signals after 20000 steps update of AMP under (a) SCAD at  $\lambda = 0.1$  and  $a = 3$  and (b) MCP at  $\lambda = 0.1$  and  $a = 3$ , where the original and reconstructed signals are represented by solid lines and circles, respectively. The system's parameters are set as (a)  $\alpha = 0.5, \rho = 0.35, N = 400$ , and (b)  $\alpha = 0.5, \rho = 0.4, N = 400$ , the parameter region of which is beyond the algorithmically reconstructable limit by the Bayes-optimal method, but the reconstruction by SCAD/MCP minimization is theoretically possible. We set the initial condition of AMP as the OLS estimator denoted by  $\hat{\mathbf{x}}^{(0)} = A^+ \mathbf{y}$ , where  $A^+$  is the pseudo inverse matrix of  $A$ . AMP's trajectory diverges when nonconvexity parameters are small, but damping factors suppress the divergence and lead to a stable update of the estimates. Even with damping factors, the naive update of AMP does not achieve

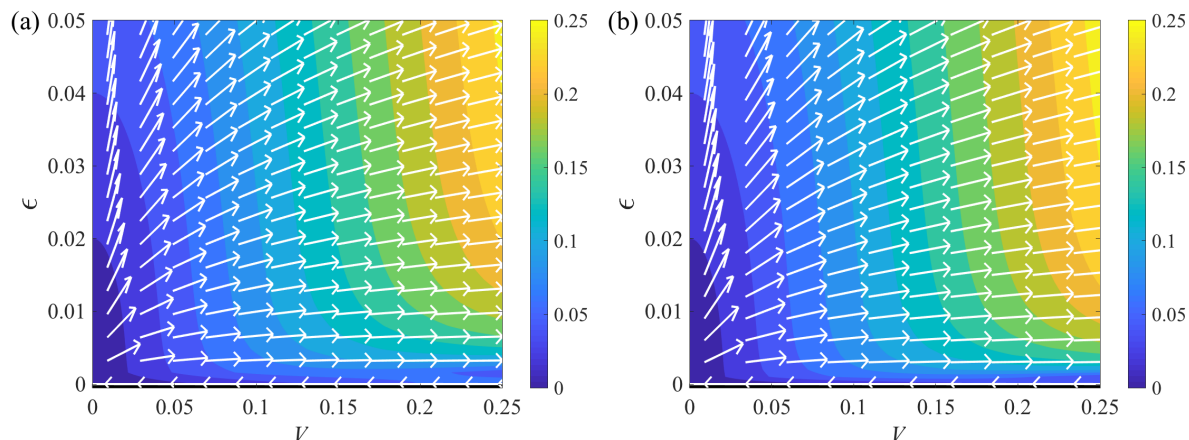


**Figure 10.** Flow of state evolution at  $\lambda = 0.1$  and  $a = 3$  of (a) SCAD for  $\alpha = 0.5$ ,  $\rho = 0.35$  and (b) MCP for  $\alpha = 0.5$ ,  $\rho = 0.4$ . The region  $10^{-4} \leq \varepsilon < 0$  is shown in black for the visibility of the arrows close to  $V$ -axis.

the perfect reconstruction shown in Figure 9, contrary to the replica predictions. The discrepancy between the replica analysis and AMP appears, in particular, when the signal is dense and a fine-tuning of the nonconvexity parameters is required.

For understanding the difficulty in achieving the perfect reconstruction of the signal by AMP at a small nonconvexity parameter region, we use state evolution (SE) [21]. Assuming that  $\hat{V}_\mu^{(t)}$  converges to  $\hat{V}^{(t)} \equiv \sum_\mu \hat{V}_\mu^{(t)} / M$  for sufficiently large  $N$  and  $M$ , the typical trajectory of AMP is characterized by two parameters  $V^{(t)} \equiv E_{\mathbf{x}^0, A}[\hat{V}^{(t)}]$  and  $\varepsilon^{(t)} \equiv E_{\mathbf{x}^0, A}[\hat{\varepsilon}^{(t)}]$ , where  $\hat{\varepsilon}^{(t)} \equiv \sum_{i=1}^N (\hat{x}_i^{(t)} - x_i^0)^2 / N$  is the mean squared error at  $t$ -th iteration step. In particular, when the components of  $A$  are independently and identically distributed with mean 0 and variance  $1/N$ , as for the Gaussian measurement matrix, the time evolution of  $V^{(t)}$  and  $\varepsilon^{(t)}$  is described by SE equations [13, 17]

$$V^{(t+1)} = \int dx^0 P_0(x^0) \int Dz \Sigma(\alpha^{-1} V^{(t)}, x^0 + z \sqrt{\alpha^{-1} \varepsilon^{(t)}}), \quad (66)$$

$$\varepsilon^{(t+1)} = \int dx^0 P_0(x^0) \int Dz \left[ \hat{x}(\alpha^{-1} V^{(t)}, x^0 + z \sqrt{\alpha^{-1} \varepsilon^{(t)}}) - x^0 \right]^2, \quad (67)$$

where  $\hat{x}(s, w) = \Sigma_p(s, w) \mathcal{M}_p(s, w)$  for  $p \in \{\text{SCAD}, \text{MCP}\}$ . SE is equivalent to the RS saddle point equation, and the fixed point denoted by  $V^*$  and  $\varepsilon^*$  correspond to the RS saddle point as  $V^* = \chi$  and  $\varepsilon^* = Q - 2m + \rho \sigma_x^2$ , respectively. Hence, the success solution is described as  $V^* = \varepsilon^* = 0$  in the SE. For any parameter region, solutions other than the success solution can appear, but their AT condition is always violated, as mentioned in Sec. 3. Note that the flow of the SE describes the typical trajectory of the AMP with respect to  $A$  and  $\mathbf{x}^0$ . Hence, it does not necessarily describe a trajectory under a fixed realization of  $A$  and  $\mathbf{x}^0$ . However, it is expected that the trajectories converge to the flow of SE for a sufficiently large system size. Hence, SE flow supports an understanding of a trajectory of AMP under a fixed set of  $A$  and  $\mathbf{x}^0$  [22].

Figure 10 shows the flow of SE at  $\lambda = 0.1$  and  $a = 3$  for (a) SCAD at  $\alpha = 0.5$ ,  $\rho = 0.35$  and (b) MCP at  $\alpha = 0.5$ ,  $\rho = 0.4$ , which have the same settings as in Figure 9.

Label $k$	Nonconvexity parameters	Initial step $t_{\text{ini}}(k)$	Final step $t_{\text{fin}}(k)$
1	$\lambda = 1, a = 10$	0	2345
2	$\lambda = 0.5, a = 10$	2346	5700
3	$\lambda = 0.5, a = 5$	5701	10105
4	$\lambda = 0.3, a = 5$	10106	14649
5	$\lambda = 0.1, a = 3$	14650	20000

**Table 1.** Controlling schedule of nonconvexity parameters for SCAD used in the reconstruction corresponding to Figure 11.

The arrows assigned to the coordinate  $(\hat{V}, \hat{\varepsilon})$  indicate the direction of SE's flow. The normalized vector of  $(V^{(t+1)} - V^{(t)}, \varepsilon^{(t+1)} - \varepsilon^{(t)})$  with  $V^{(t)} = \hat{V}$  and  $\varepsilon^{(t)} = \hat{\varepsilon}$ , and their actual magnitudes are depicted in colour. As shown in Figure 10, most of the SE flow leads to a divergence of  $V$  and  $\varepsilon$ ; however, there is still a region close to the  $V$ -axis where the flows are directed to  $V = \varepsilon = 0$ . This region shrinks to  $V$ -axis as the nonconvexity parameter decreases. Furthermore, the gradient in this region approaches zero. Therefore, the possibility that AMP attains the success solution  $V = \varepsilon = 0$  from arbitrary initial conditions is exceedingly small. The shrinking basin and vanishing gradient are the origin of the difficulty of AMP for small nonconvexity parameters.

To resolve this problem, we recall that a failure solution appears for  $\alpha < \alpha_c$  for large nonconvexity parameters, as discussed in Figs. 7 and 8. The emergence of a failure solution implies that the SE has a locally stable fixed point from the correspondence between the saddle point of RS free energy and the SE. However, the failure solution for  $\alpha < \alpha_c$  does not satisfy the AT stability condition, which is equivalent to the local stability of AMP. Therefore, AMP for large nonconvexity parameter does not converge to a fixed point, but its trajectory is confined into a subshell characterized by finite  $\varepsilon$  and  $\chi$ . We utilize this nondivergence property of AMP in  $\alpha < \alpha_c$  at sufficiently large nonconvexity parameters for the perfect reconstruction of dense signals at small nonconvexity parameters. The procedure introduced here, based on the above consideration is termed as *nonconvexity control*, where we decrease the value of nonconvexity parameters in updating AMP.

We explain the effect of nonconvexity control using the SE's flow for SCAD shown in the left panels of Figure 11, where  $A$  and  $\mathbf{x}^0$  are the same as those used in Figure 9 (a). The controlling schedule of nonconvexity parameters demonstrated here is summarized in Table 1. The values of nonconvexity parameters are labelled as  $k$ , and  $t_{\text{ini}}(k)$  and  $t_{\text{fin}}(k)$  represent the initial step and final step of AMP, respectively, where  $k$ -th nonconvexity parameters are used. The square and circle points in the left panels of Figure 11 indicate the values of  $\hat{V}^{(t)}$  and  $\hat{\varepsilon}^{(t)}$  at  $t = t_{\text{ini}}(k)$  and  $t = t_{\text{fin}}(k)$ , respectively. At the first value of nonconvexity parameters  $\lambda = 1, a = 10$ , SE has a fixed point corresponding to a failure solution that violates the AT condition, which is denoted by a star in the left panel of Figure 11 (a). One can approach a small  $\varepsilon$  and  $V$  region from the initial condition given by the OLS estimator, utilizing the rotational flow around



the fixed point. As the values of the nonconvexity parameters decrease, the fixed point corresponding to the failure solution diverges, but, fortunately, there exists a weak flow directed to  $(V, \varepsilon) \rightarrow (0, 0)$  in small  $\varepsilon$  and  $V$  region (Figure 11 (b)), although the success solution does not exist. When the success solution becomes the stable solution for sufficiently small nonconvexity parameters, the region with flows directed to  $V = \varepsilon = 0$  becomes the basin of attraction to the success solution. By nonconvexity control, one can gradually move the estimates in AMP to be on the basin of attraction of the success solution, and finally obtain  $V = \varepsilon = 0$  as shown in the left panel of Figure 11. The reconstructed signals  $\hat{\mathbf{x}}^{(t)}$  for  $t = t_{\text{fin}}(k)$  (circles) are compared with the original signal  $\mathbf{x}^0$  (solid lines) in the right panels of Figure 11. Comparing Figure 9 (a) and the right panel of Figure 11 (c), the performance of the reconstruction is considerably improved, and the perfect reconstruction is achieved by the nonconvexity control. Note that the examined parameter values of  $\alpha$  and  $\rho$  here exceed the algorithmic limit of the Bayes-optimal setting. Thus, the result here demonstrates that the signal reconstruction using the piecewise continuous penalties outperforms that by using the Bayes-optimal framework.

The time evolution of  $\hat{V}^{(t)}$  and  $\hat{\varepsilon}^{(t)}$  in AMP of SCAD minimization with and without controlling nonconvexity parameters are compared in Figure 12. The time steps of the nonconvexity parameters' change are indicated by the arrows. When the control of nonconvexity parameters is not introduced, the values of  $\hat{V}^{(t)}$  and  $\hat{\varepsilon}^{(t)}$  in AMP with appropriate damping saturate at a certain value larger than zero. However, starting from large nonconvexity parameters, their values can be decreased gradually, and finally  $\hat{V}^{(t)} \rightarrow 0$  and  $\hat{\varepsilon}^{(t)} \rightarrow 0$  is achieved at a sufficiently large  $t$ .

The properties of the SE flow in MCP are similar to that in SCAD. A controlling schedule of nonconvexity parameters for MCP is summarized in Table 2, and corresponding SE flow and reconstructed signals are shown in Figure 13. The time evolution of  $\hat{V}^{(t)}$  and  $\hat{\varepsilon}^{(t)}$  with and without nonconvexity control are compared in Figure 14. As with SCAD, utilizing the nonconvexity control, The estimates of AMP gradually approaches  $\hat{V}^{(t)} \rightarrow 0$  and  $\hat{\varepsilon}^{(t)} \rightarrow 0$ .

To reconstruct denser signals close to  $\rho = \alpha$ , we need to tune nonconvexity parameters to smaller values,  $\lambda \rightarrow 0$  and  $a \rightarrow a_{\text{min}}$ . However, the basin of the attraction to the success solution is almost on the axis  $V$  for such small nonconvexity parameters, and infinitesimal deviations from the basin is not allowed. For the perfect reconstruction close to  $\rho = \alpha$ , we must carefully design the schedules of the nonconvexity control, considering the continuity of the basin structures with respect to the nonconvexity parameters. Even when  $\rho = \alpha$ , the failure solution exists for sufficiently large nonconvexity parameters, and it can be a guide for the perfect reconstruction. Annealing the values of the nonconvexity parameters in signal reconstruction is a possible solution to achieve fine tuning. In the linear regression problems with piecewise nonconvex penalties, annealing of the nonconvexity parameters is efficient for obtaining a stable solution path and the associated cross-validation error [23]. Further, monitoring the time evolution of  $\varepsilon$  is significant for an efficient controlling. However, the quantity  $\hat{\varepsilon}^{(t)}$  is not observable, as we do not know the original signal in realistic settings. One needs

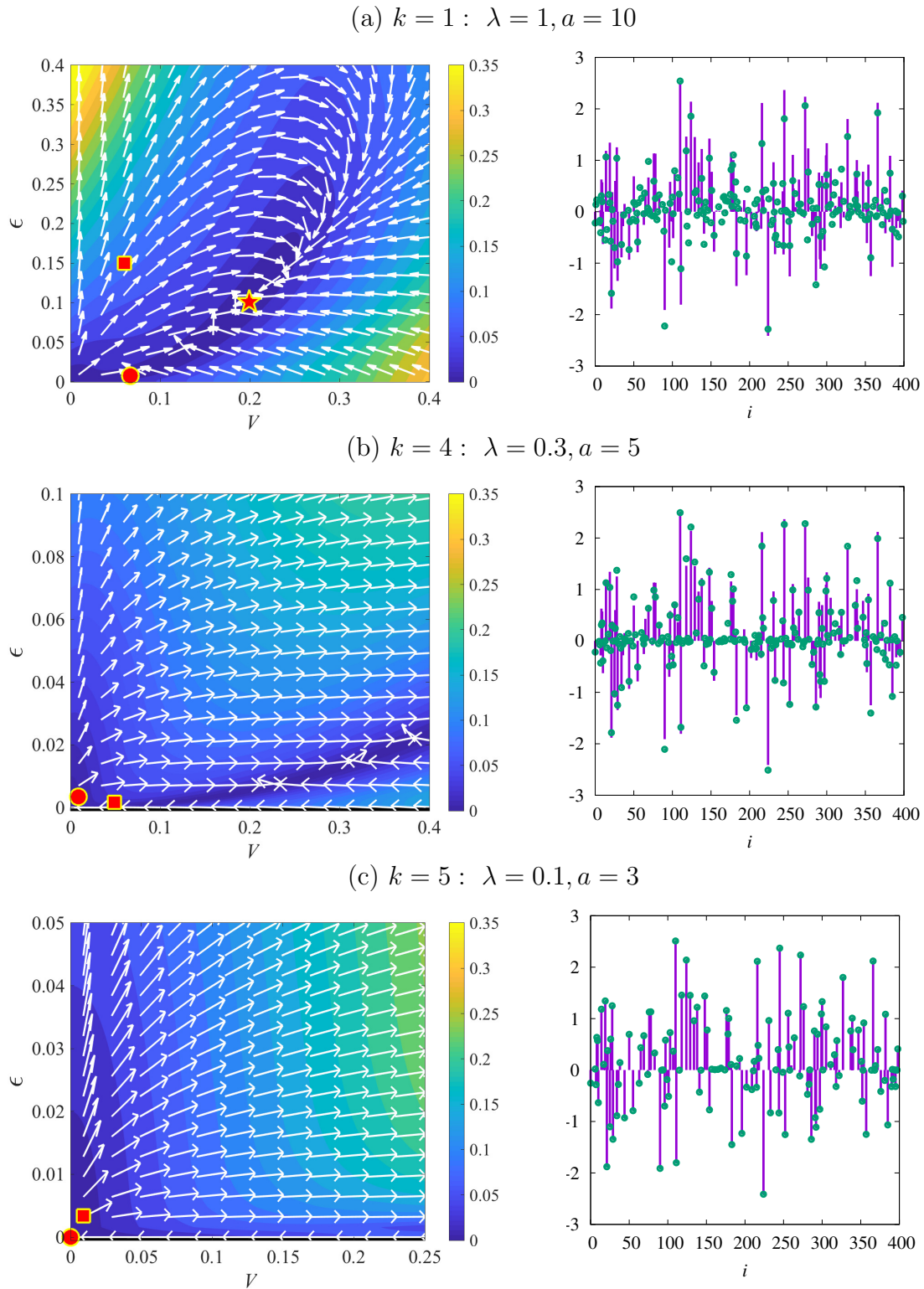


**Figure 11.** **Left:** Direction and gradients of SE's flows for SCAD.  $\blacksquare$  and  $\bullet$  are the states for  $t_{\text{ini}}(k)$  and  $t_{\text{fin}}(k)$  for  $k$ -th nonconvexity parameters, respectively.  $\star$  in (a) is the fixed point of SE. **Right:** Comparison of  $\mathbf{x}^0$  (solid line) and the reconstructed signals for  $t_{\text{fin}}(k)$  (circles). The region  $10^{-3} \leq \epsilon < 0$  in the left figures of (b) and (c) are shown in black for the visibility of arrows on the  $V$ -axis.

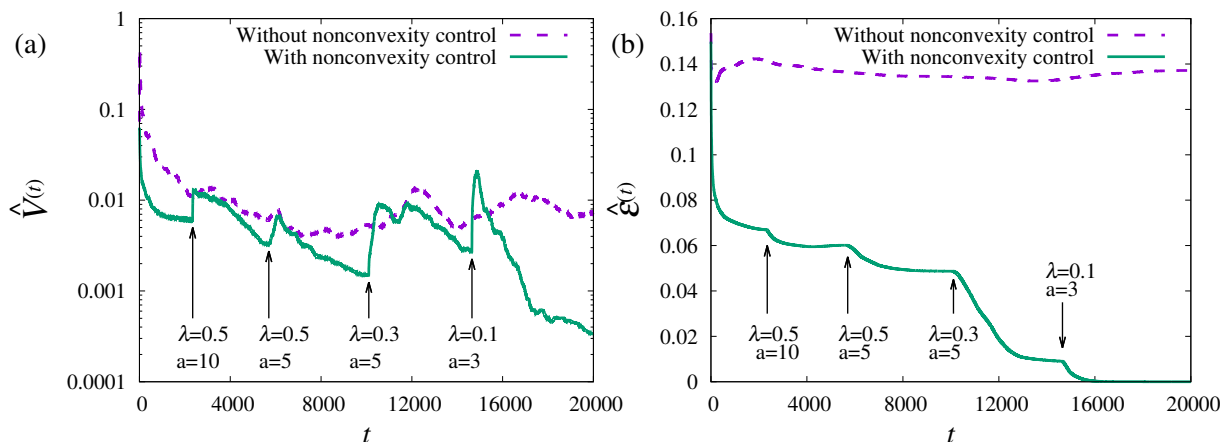


**Figure 12.** Time evolution of (a)  $\hat{V}^{(t)}$  and (b)  $\hat{\varepsilon}^{(t)}$  in AMP under SCAD minimization for  $\alpha = 0.5$ ,  $\rho = 0.35$ , and  $N = 400$ . The nonconvexity parameter for non-controlled case is  $\lambda = 0.1$  and  $a = 3$ . In the controlled case, the controlling schedule is shown in Table 1, and  $t_{\text{ini}}(k)$  are indicated by arrows.

Label $k$	Nonconvexity parameters	Initial step $t_{\text{ini}}(k)$	Final step $t_{\text{fin}}(k)$
1	$\lambda = 1, a = 10$	0	4545
2	$\lambda = 0.5, a = 10$	4546	7873
3	$\lambda = 0.5, a = 5$	7874	13042
4	$\lambda = 0.1, a = 3$	13043	20000

**Table 2.** Controlling schedule of nonconvexity parameters for MCP used in reconstruction corresponding to Figure 13 (b).

to develop an appropriate estimator for  $\varepsilon$ , and further research is a promising direction of future work.

## 6. Summary and discussion

We have analytically derived the perfect reconstruction limit of the sparse signal in compressed sensing by the minimization of nonconvex sparse penalties, SCAD and MCP. In particular, when the nonconvexity parameters are small, SCAD and MCP minimization reconstruct dense signals that are beyond the  $\ell_1$  reconstruction limit and algorithmic limit of the Bayes-optimal method. The theoretically derived reconstruction limit was not achieved by simply applying AMP when the signal to be reconstructed is relatively dense; however, the performance was considerably improved by associating it with the control of the nonconvexity parameters. By observing the SE's flow, it was found that the difficulty of AMP for small nonconvexity parameters is caused by the shrinking basin of attraction and the vanishing gradient on the basin. We show that a non-negligible portion of this difficulty is resolved by the nonconvexity control that connects the trajectory of AMP for large nonconvexity parameter to the basin of attraction to the success solution that appears for small nonconvexity parameters. A

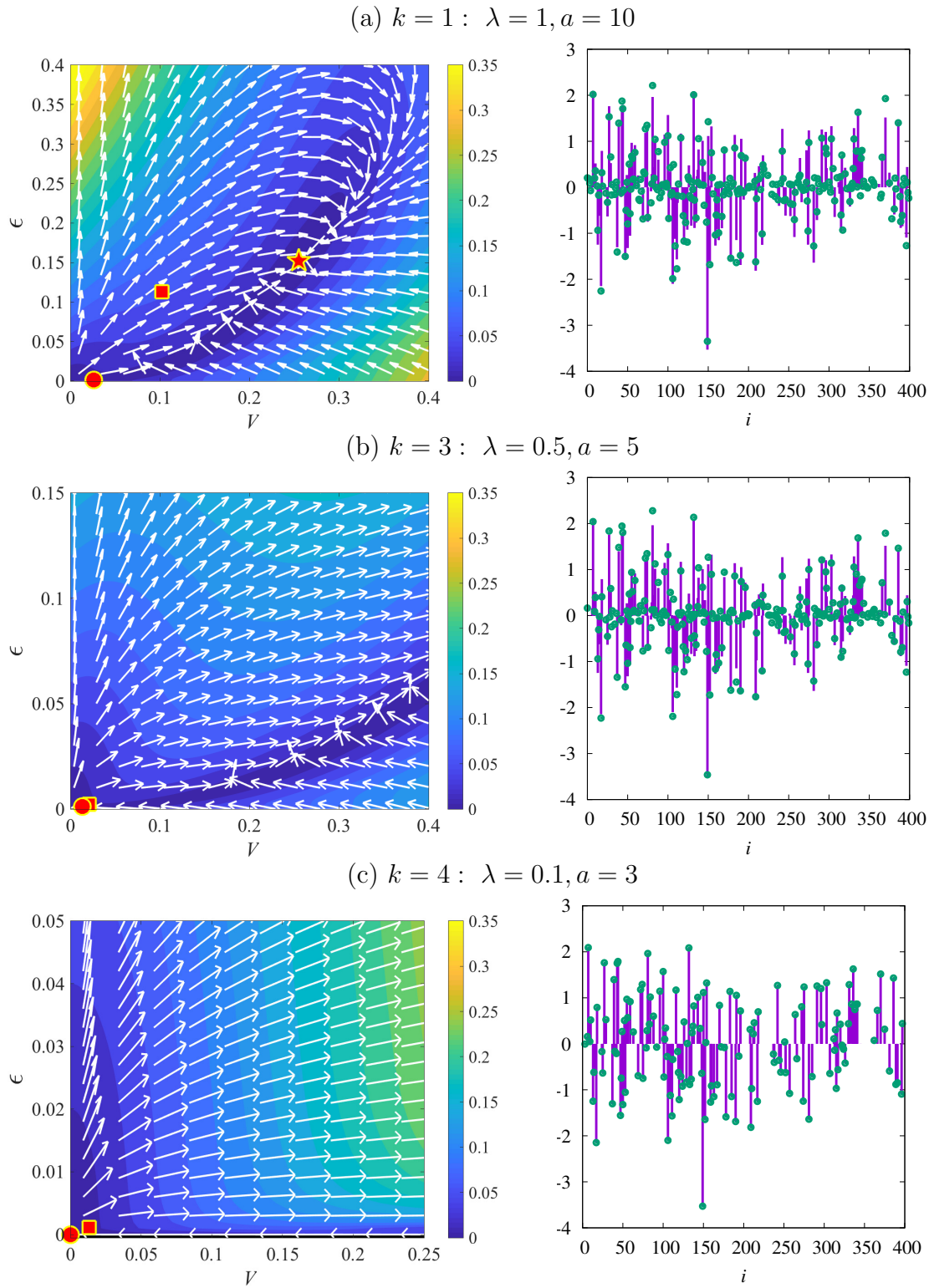


**Figure 13.** **Left:** Direction and gradients of SE's flows for MCP.  $\blacksquare$  and  $\bullet$  are the states for  $t_{\text{ini}}(k)$  and  $t_{\text{fin}}(k)$  for  $k$ -th nonconvexity parameters, respectively.  $\star$  in (a) is the fixed point of SE. **Right:** Comparison of  $\mathbf{x}^0$  (solid line) and the reconstructed signals for  $t_{\text{fin}}(k)$  (circles). The region  $10^{-3} \leq \epsilon < 0$  in the left figure of (c) is shown in black for the visibility of arrows on the  $V$ -axis.

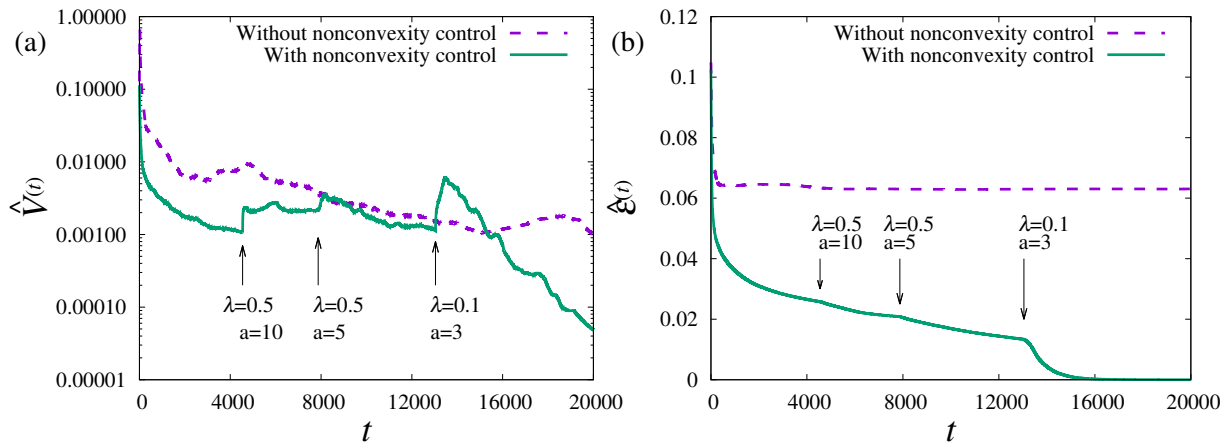


**Figure 14.** Time evolution of (a)  $\hat{V}^{(t)}$  and (b)  $\hat{\varepsilon}^{(t)}$  in AMP under MCP minimization for  $\alpha = 0.5$ ,  $\rho = 0.4$ , and  $N = 400$ . The nonconvexity parameter for non-controlled case is  $\lambda = 0.1$  and  $a = 3$ . In the controlled case, the controlling schedule is shown in Table 2, and  $t_{\text{ini}}(k)$  are indicated by arrows.

more detailed research on an appropriate controlling schedule that can be applied to sufficiently small  $\lambda$  is an issue for future work.

Originally, SCAD and MCP were designed to satisfy the continuity and the oracle property, which is the simultaneous appearance of the asymptotic normality and consistency, at a certain limit with respect to the nonconvexity parameters [11, 12]. However, such property is not sufficient for practical usage. The design of the nonconvex penalties that does not lead to a shrinkage of basin and vanishing gradient is another possibility for nonconvex compressed sensing. First, a quantitative comparison between SCAD and MCP should be studied. We have observed that the possible nonconvexity parameter region for the perfect reconstruction in MCP is larger than that in SCAD, and in this sense MCP is better than SCAD. The relationship between the degrees of freedom of nonconvexity parameters, the shrinking basin, and vanishing gradient should be clarified.

## Acknowledgments

The authors would like to thank Yoshiyuki Kabashima, Satoshi Takabe, Mirai Tanaka, and Yingying Xu for their helpful discussions and comments. This work is partially supported by JSPS KAKENHI No. 16K16131 (AS), and Nos. 18K11463 and 17H00764 (TO). TO is additionally supported by a Grant for Basic Science Research Projects from the Sumitomo Foundation.

## References

- [1] Candés E J and Tao T 2006 *IEEE transactions on information theory* **52** 5406–5425
- [2] Donoho D L 2006 *IEEE Transactions on information theory* **52** 1289–1306
- [3] Chen S S, Donoho D L and Saunders M A 2001 *SIAM Review* **43** 129–159

- [4] Tropp J A 2007 *IEEE Transaction on Information Theory* **53** 4655–4666
- [5] Donoho D L, Maleki A and Montanari A 2011 *IEEE Transaction on Information Theory* **57** 6920–6941
- [6] Chartrand R and Yin W 2008 Iteratively reweighted algorithms for compressive sensing *IEEE International Conference on Acoustics, Speech and Signal Processing (IEEE)* pp 3869–3872
- [7] Gribonval R and Nielsen M 2003 *IEEE Transaction on Information Theory* **49** 3320
- [8] Candés E J 2008 *Comptes Rendus Mathématique* **346** 589–592
- [9] Chartrand R 2007 *IEEE Signal Process. Lett.* **14** 707–710
- [10] Chartrand R and Staneva S 2008 *Inverse Problems* **24** 035020
- [11] Fan J and Li R 2001 *Journal of the American statistical Association* **96** 1348–1360
- [12] Zhang C H 2010 *The Annals of Statistics* **38** 894–942
- [13] Sakata A and Xu Y 2018 *J. Stat. Mech.* **2018** 033404
- [14] Donoho D L 2006 *Discrete & Computational Geometry* **35** 617–652
- [15] Donoho D L and Tanner J 2009 *Journal of American Mathematical Society* **22** 1–53
- [16] Kabashima Y, Wadayama T and Tanaka T 2009 *Journal of Statistical Mechanics: Theory and Experiment* **2009** L09003
- [17] Krzakala F, Mézard M, Sausset F, Sun Y and Zdeborová L 2012 *Journal of Statistical Mechanics: Theory and Experiment* **2012** P08009
- [18] De Almeida J and Thouless D J 1978 *Journal of Physics A: Mathematical and General* **11** 983
- [19] Sakata A 2018 *J. Stat. Mech.* **2018** 063404
- [20] Obuchi T, Nakanishi-Ohno Y, Okada M and Kabashima Y 2018 *J. Stat. Mech.* **2018** 103401
- [21] Mezard M and Montanari A 2009 *Information, physics, and computation* (Oxford University Press)
- [22] Bayati M and Montanari A 2011 *IEEE Transaction on Information Theory* **57** 764–785
- [23] Obuchi T and Sakata A 2019 Cross validation in sparse linear regression with piecewise continuous nonconvex penalties and its acceleration (in preparation)